Chapter 5

Synthesis of Conductive Sol-Gel ZnO Films and Development of ZnO Printed Electronics

David Winarski and Farida Selim

Additional information is available at the end of the chapter

http://dx.doi.org/10.5772/intechopen.82041

Abstract

ZnO thin films are synthesized and studied to understand the functionality of solution-processed semiconductor devices. A simple sol-gel technique is used to fabricate transparent conductive oxides (TCOs) and ultraviolet (UV) photodetectors from ZnO precursors via spin coating, inkjet printing (IJP), and aerosol jet printing (AJP). A variety of flexible and transparent substrates was selected based on the deposition and sintering conditions and the device application. Doping of ZnO films with Al^{3+}, In^{3+}, and Ga^{3+} was introduced in precursor solutions before deposition processes. Post-deposition processing was carried out in air, H_2, and Zn environments to optimize thin film properties. Optical, structural, and electronic data analyses reveal the significant effects that deposition method, substrates, dopants, and processing conditions have on the optical transmission, crystallinity, grain size, and electrical conductivity.

Keywords: flexible electronics, zinc oxide, UV photodetectors, aerosol jet printing, inkjet printing, vacancy passivation, positron annihilation spectroscopy

1. Introduction

Printing electrically functional inks has emerged as an important research topic to drive device technologies into the future. It has some advantages compared to conventional fabrication techniques in terms of low cost and applicability for flexible devices. This is promising for wearable, implantable, patch-like, and textile-integrated electronics, advancing the device field. With the right ink and substrate, it would be possible to achieve lightweight, flexible, transparent devices with a good electrical performance, which will revolutionize our daily lives.

Until recently, organic inks have monopolized printing technology because of their printability, flexibility, and electronic functionality. However, developing printable inorganic inks would allow for higher performance—like conventional devices—at a much lower cost than conventional fabrications, such as atomic layer deposition (ALD), pulsed laser deposition (PLD), chemical vapor deposition (CVD), physical vapor deposition (PVD), molecular beam epitaxy (MBE), and sputtering. In addition, printing techniques allow for deposition at low temperatures and at specified locations, a controllability of both parameters that no other deposition techniques can claim. These advantages make printing much easier and more compatible with flexible substrates, as some polymers cannot withstand the high processing temperatures of some deposition techniques or the harsh chemicals and UV radiation in the photolithography necessary to construct a functional device.

Some facile printing technologies are inkjet (IJP) and aerosol jet printing(AJP). Inkjet printing (IJP) is very quick and a simple drop-on-demand or continuous stream technique with micrometer precision [1, 2]. Aerosol jet printing (AJP) is favored as a clean and precise technique, using a continuous stream to print features down to 10 μm [3]. Nonetheless, both techniques are new and exciting ways to fabricate electronic devices. Both AJP and IJP techniques are currently used to print a wide variety of organic and inorganic inks for use as flexible photodetectors, transistors, and other circuit board components [4–10]. ZnO is an exciting material for electronics due to its direct wide bandgap (3.2 eV at 298 K), strong UV absorption, and electrical tunability. Many researchers have successfully fabricated ZnO devices at low cost and relatively low temperature by way of printing sol-gel precursor and other nanoparticle-based inks [11–20]. In addition, the authors of this chapter have successfully fabricated ZnO transparent conductive oxides (TCOs) using a simple sol-gel, spin coating technique [21]. Research efforts utilizing sol-gel-derived ZnO thin films for device applications have greatly increased, recently [22–24]. Through these methods, the resultant ZnO material properties can be tuned by introducing group III metal ions during the precursor sol synthesis. In this chapter, we present the use of a sol-gel technique to develop ZnO printed electronics.

To understand the applications of ZnO sol-gel precursors, we employ spin coating, IJP, and AJP deposition with thermal and photonic sintering to synthesize and tune ZnO thin films. Extrinsic shallow donors, such as Al^{3+}, In^{3+}, and Ga^{3+}, have similar ionic radius to that of Zn^{2+} and thus can easily replace it with little effect on the lattice structure [20, 25–29]. These donors are introduced during the precursor solutions' synthesis and various atmospheric post-processing heat treatments are applied to introduce, eliminate, or passivate intrinsic defects that greatly alter the electrical conductivity of the films. The ZnO thin film properties are studied by scanning electron microscopy (SEM), X-ray diffraction (XRD), ultraviolet-visible range (UV-VIS) absorbance, Van der Pauw and Hall effect measurements, and positron annihilation spectroscopy (PAS).

2. Sol-gel synthesis

To make a ZnO sol-gel precursor, we dissolve zinc acetate (99.99%) in 2-methoxyethanol (99.8%)—using ethanolamine (99%) as a stabilizer—to obtain a 0.75 M solution, with zinc acetate and ethanolamine at a 1:1 molar ratio. To dope ZnO thin films, aluminum(III) nitrate nonahydrate (99.997%), gallium(III) nitrate hydrate (99.9998%), and indium(III) acetate

http://dx.doi.org/10.5772/intechopen.82041

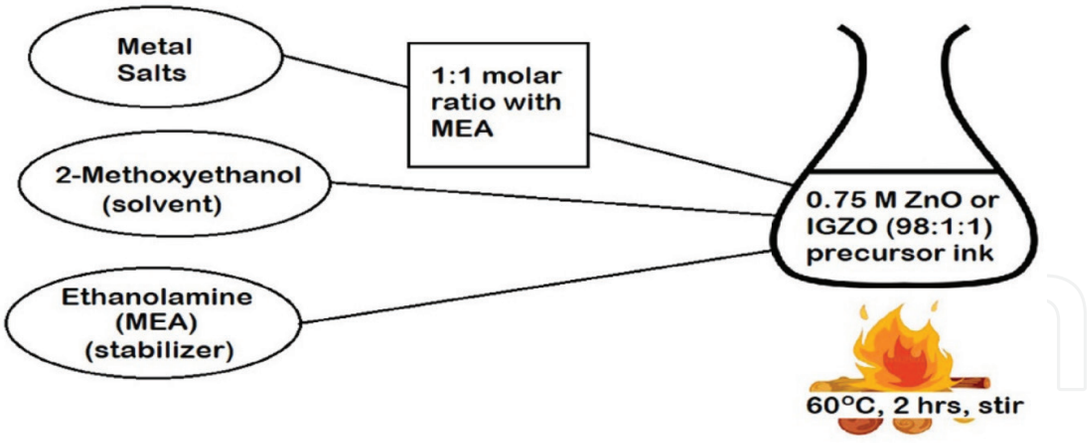

Figure 1. Synthesis procedure for ZnO, AZO, GZO, and IGZO precursor solutions.

hydrate (99.99%) metal salts were implemented to replace some zinc acetate in the mixture to obtain a doping level of 1% in solution while keeping the 1:1 molar ratio with ethanolamine and the molarity at 0.75 M. Undoped ZnO, aluminum-doped ZnO (AZO), gallium-doped ZnO (GZO), and indium-gallium-codoped ZnO (IGZO) precursor solutions were prepared in an open-air environment, then covered with plastic paraffin film, heated to 60°C, and magnetically stirred for 2 h to obtain a transparent homogenous solution and then left to cool before deposition (**Figure 1**).

3. Substrate preparation: piranha etching and atmospheric plasma treatment

Quartz, cyclic olefin copolymer (TOPAS), polyethylene terephthalate (PET), and polyimide (Kapton) substrates were selected based on their transparency and/or flexibility. Before ZnO deposition, substrates were cleaned and etched to improve substrate/solution compatibility. Quartz substrates were treated in piranha baths to clean residual contaminants from the substrate and induce a surface charge. The substrate was placed in a 3:1 H_2SO_4:H_2O_2 bath at 80°C for 15 min, rinsed with deionized water, placed in a 3:1 NH_4OH:H_2O_2 bath at 80°C for 15 min, rinsed with deionized water again, and placed in an oven at about 100°C to dry. Before IJP and AJP, quartz, TOPAS, PET, and Kapton substrates were prepared by swabbing with acetone and isopropanol, drying with a nitrogen gun, and applying atmospheric plasma treatment from a corona discharge wand with the transformer set at 200 W at a standoff distance of 5 mm from the ground electrode.

4. Thin film synthesis

Once the sol-gel precursors and substrates have been prepared, ZnO thin films were deposited using spin coating, IJP, and AJP. **Table 1** summarizes ZnO sol-gel precursors, substrates, deposition methods, sintering conditions, and post-processing environments and thicknesses.

4.1. Spin coating

A Laurell Technologies Corporation spin coater was used to spin a quartz substrate at 500 rpm. Then, 40–50 drops of precursor solution were dispensed, before the substrate/solution was accelerated to 3000 rpm and left spinning for 30 s to obtain a gel-like thin layer. Next, the gel film was placed in an oven to dry at 150°C for 10 min. The spin coating and drying processes were repeated to obtain the desired number of layers (10–16 layers total). Finally, the films were annealed in ambient air at 400°C for 60 min, to obtain a ZnO wurtzite structure. ZnO, AZO, and GZO films were fabricated using this spin coating technique. To tune the electronic properties, several samples were further annealed in the following flowing gas conditions: (1) forming gas of 95% N_2 and 5% H_2 at 400°C for 60 min, (2) H_2 flow at 400°C for 60 min, and (3) Zn-rich environment in Ar at 400°C for 60 min. The Zn-rich environment was created with Zn powder (99.999%) and Zn foil (99.994%, 0.1 mm thick). Thin films and Zn powder were wrapped tightly in Zn foil, while an Ar gas flow was used to prevent oxidation of the ZnO.

4.2. Inkjet printing

A Dimatix inkjet printer printed 7 mm × 7 mm squares of ZnO and IGZO sol-gel precursors onto various substrates for a total of 12 layers. The jet and platen temperatures were set to

Sample	Substrate	Deposition method	Sintering conditions	Thickness (nm)
GZO	Quartz	Spin coating	400°C, 60 min, air	800
GZO	Quartz	Spin coating	400°C, 60 min, air	808
AZO	Quartz	Spin coating	400°C, 60 min, air	515
ZnO^0	Quartz	Spin coating	400°C, 60 min, air	600
ZnO^0	Quartz	Spin coating	400°C, 60 min, air	173
ZnO^1	TOPAS	Inkjet printing	170°C, 60 min, air	~600
ZnO^2	Kapton	Inkjet printing	300°C, 20 min, air	~600
ZnO^3	TOPAS	Inkjet printing	Xenon, 180 bursts, N_2	~600
ZnO^3	Kapton	Inkjet printing	Xenon, 180 bursts, N_2	~600
ZnO^3	PET	Inkjet printing	Xenon, 180 bursts, N_2	~600
ZnO^4	TOPAS	Inkjet printing	150°C, 30 min, air	~600
ZnO^4	Kapton	Inkjet printing	150°C, 30 min, air	~600
ZnO^5	Kapton	Inkjet printing	400°C, 60 min, air	~600
ZnO^6	Kapton	Aerosol jet printing	200°C, 60 min, air	~400
ZnO^7	Kapton	Aerosol jet printing	300°C, 60 min, air	~400
ZnO^8	Kapton	Aerosol jet printing	400°C, 60 min, air	~400
$IGZO^1$	Quartz	Inkjet printing	400°C, 60 min, air	~600
$IGZO^2$	Kapton	Inkjet printing	400°C, 60 min, air	~600
$IGZO^3$	Kapton	Aerosol jet printing	400°C, 60 min, air	~400

Table 1. A summary of ZnO sol-gel precursors, substrates, deposition methods, sintering conditions, and post-processing environments and thicknesses. Thicknesses were evaluated by SEM, ellipsometry, and profilometry techniques [20, 21].

39°C, and the droplet overlap was set to at least 50%. The droplet size was between 50 and 100 μm, depending on the substrate. The resultant gels were dried at 150°C for 10–30 min (until visibly dry) to remove any residual solvent. Here, processing techniques were limited by the thermal expansion coefficient of the substrates. Post-print sintering was carried out using thermal and photonic sintering methods. Thermal sintering took place in ambient atmosphere on a hot plate at temperatures between 170 and 400°C for 20–60 min. Photonic sintering was carried out in a N_2-rich atmosphere using a xenon arc lamp placed 4.445 cm above the substrate platen, set at 2 kV with 6-ms pulse width for a total of 180 bursts.

4.3. Aerosol jet printing

An Optomec aerosol jet printer printed similar 7 mm × 7 mm squares of ZnO sol-gel precursors onto Kapton substrates for a total of six layers. A 200-μm nozzle was used at a speed of 3 mm/s. The line width of the aerosol spray was about 75 μm, so a 50-μm serpentine pattern was selected to achieve ~33% overlap. The resultant gels were dried at 90°C for 30 min (until visibly dry), then subject to thermal sintering in ambient atmosphere on a hot plate at 200°, 300°, and 400°C for 60 min.

5. Scanning electron microscopy

Spin-coated AZO thin films that were post-processed in H_2 and Zn were imaged by SEM. Low-magnification surface images show worm-like structures (**Figure 2**), while a higher

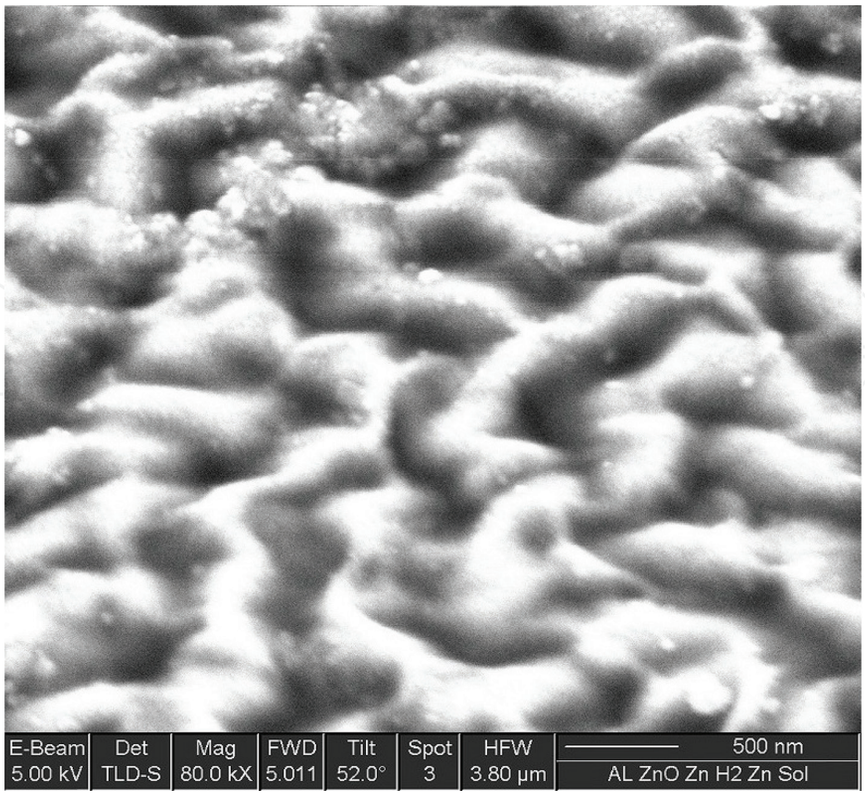

Figure 2. Low-magnification SEM surface image for AZO film deposited by spin coating and post-processed in H_2 and Zn environments, consecutively [21].

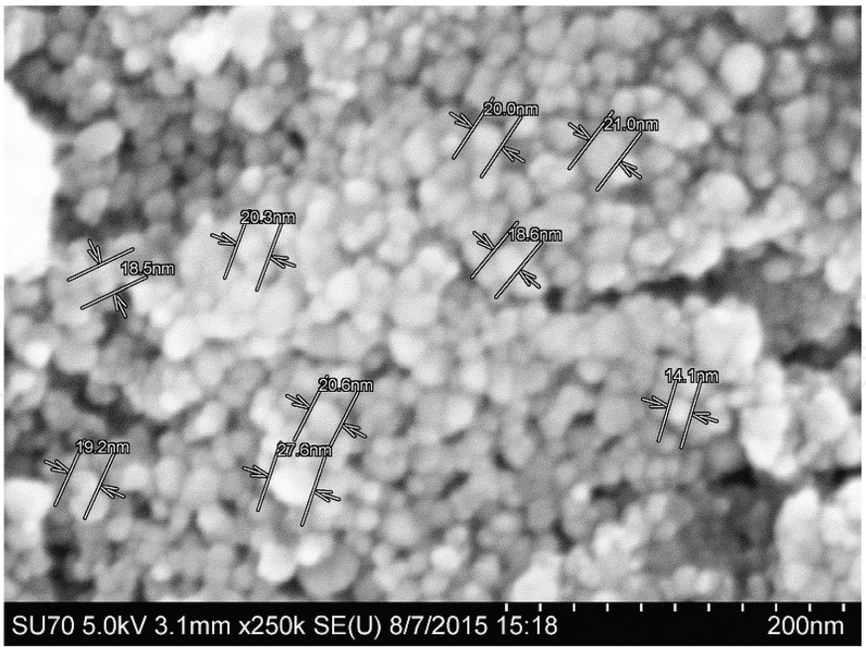

Figure 3. High-magnification SEM surface image for AZO film deposited by spin coating and post-processed in H_2 and Zn environments, consecutively [21].

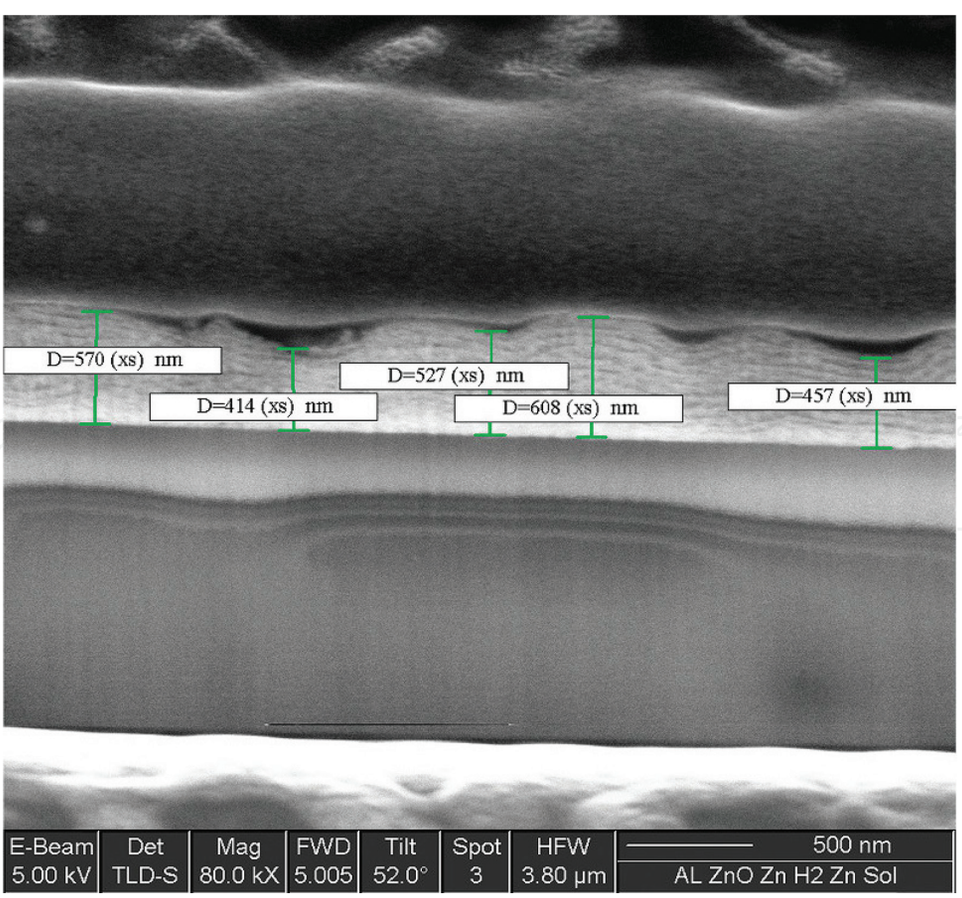

Figure 4. High-magnification cross-sectional SEM image of AZO films deposited by spin coating and post-processed in H_2 and Zn environments, consecutively [21].

http://dx.doi.org/10.5772/intechopen.82041

magnification shows round particles with an average particle size of 20 nm (**Figure 3**). Platinum was then deposited on the film surface by a focused ion beam and a trench was milled through the sample to obtain a high-resolution cross-sectional image (**Figure 4**). It can be seen that the film is deposited as distinct individual layers (each layer is ~40 nm thick). The images also reveal non-uniform thickness, with ~25% variation across the film and indicate that it is difficult to obtain uniform thickness using sol-gel methods. These images represent the first high-resolution cross-sectional images for sol-gel films. They illustrate that the distinct individual layers and the non-uniformity in thickness are inherent of the spin coating method, but they may be reduced by further annealing. This non-uniform layering leads to interference in UV-VIS transmission spectra, a well-known feature in sol-gel films.

6. X-ray diffraction

Film crystallinity was studied using a Rigaku X-ray diffractometer to determine the ZnO crystal phase (*hkl* values) and average grain size. XRD patterns for spin-coated AZO films indicate polycrystalline thin films, with peaks corresponding to the (100), (002), and (101) planes (**Figure 5**). These diffraction patterns match the ZnO hexagonal wurtzite structure, without any secondary phase impurities in the films. Furthermore, we can see a change in polycrystallinity based on post-processing in H_2 and Zn environments. When processed in H_2, films become less polycrystalline, while processing in Zn leads to the opposite effect.

XRD patterns for IJP ZnO films (**Figure 6**) reveal that ZnO phases form at temperatures as low as 150°C, with more peaks appearing at increased sintering temperature. Although there is a lack of ZnO phase formation for ZnO[4] on Kapton and an impurity phase for ZnO[3] on TOPAS,

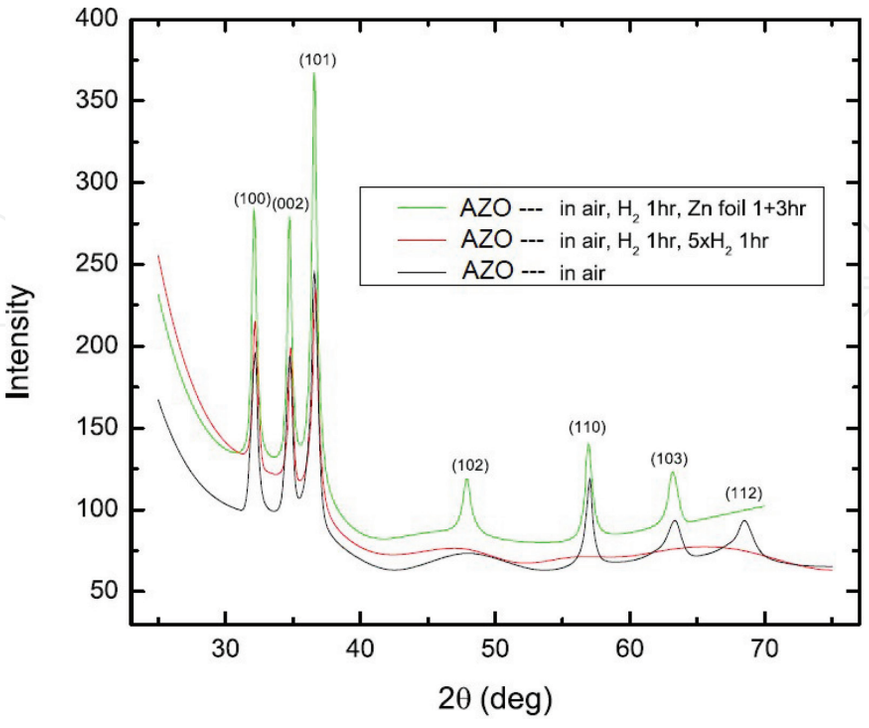

Figure 5. XRD measurements for AZO films annealed in various atmospheres [21].

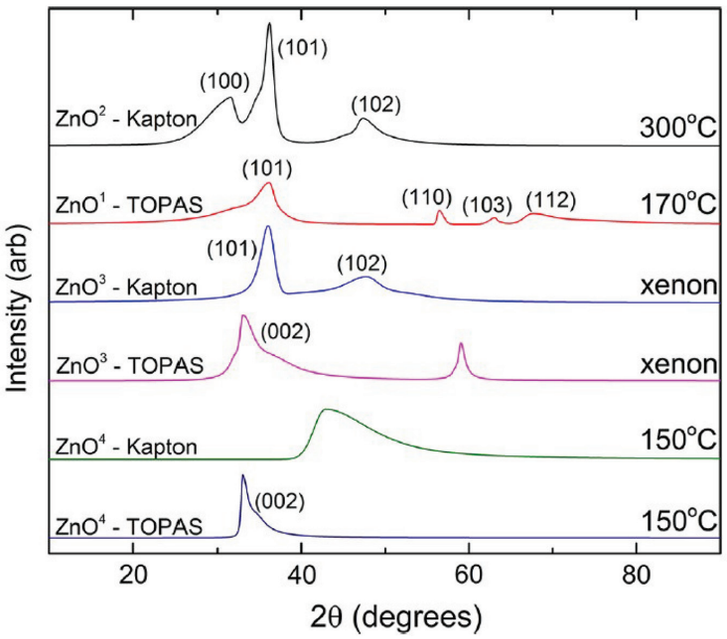

Figure 6. XRD spectra for IJP films on Kapton and TOPAS substrates sintered by hot plate and xenon arc lamp [20].

the results demonstrate that ZnO thin films can be successfully fabricated by inkjet printing and thermal and photonic sintering processes.

XRD patterns for AJP ZnO reveal amorphous nature at 200°C and an increasing polycrystallinity with the sintering temperature. In addition, increasing the sintering temperature increases the average grain size, which is consistent with previous reports [30, 31]. XRD patterns for AJP IGZO XRD show a ~50% increase in grain size due to the low doping concentration of In^{3+} and Ga^{3+}, with a minimal effect on the polycrystalline structure. **Table 2** presents the average grain sizes of the aforementioned thin films. The grain size D was calculated for each 2θ peak using the Scherrer equation:

$$D = 0.9\lambda/\beta \cos\theta, \tag{1}$$

where $\lambda = 1.54$ Å is the X-ray wavelength, β is the full width at half maximum (FWHM) of the corresponding peak, and θ is the Bragg angle.

Sample	Sintering conditions	Average grain size (Å)	Estimated standard deviation
ZnO[6]	200°C, 60 min, air	32.33	6.04
ZnO[7]	300°C, 60 min, air	239.17	36.25
ZnO[8]	400°C, 60 min, air	500.32	119.91
IGZO[3]	400°C, 60 min, air	736.84	27.85

Table 2. Average grain size—calculated by the Scherrer equation—and standard error values corresponding to ZnO and IGZO films in **Figure 7** [20].

http://dx.doi.org/10.5772/intechopen.82041

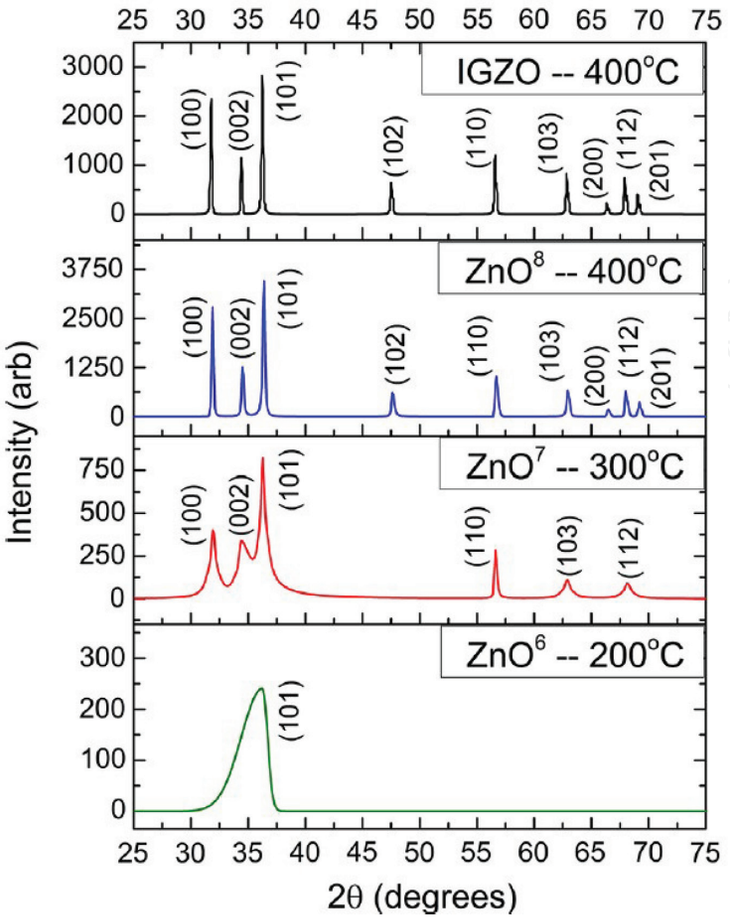

Figure 7. XRD spectra for AJP ZnO films on Kapton sintered at 200°C, 300°C, and 400°C and AJP IGZO films on Kapton sintered at 400°C [20].

ZnO, AZO, GZO, and IGZO sol-gel precursors are viable options to achieve a ZnO wurtzite structure at low sintering temperatures. Films are generally inhomogeneous in thickness and amorphous or polycrystalline in nature, with grain size and polycrystallinity increasing with the sintering temperature. A low doping concentration does not inhibit ZnO wurtzite formation, but the incorporation of In^{3+} and Ga^{3+} dopants effectively increases the average grain size. Furthermore, post-processing in H_2 and Zn environments can change the polycrystallinity of the films.

7. Ultraviolet-visible range spectroscopy

A dual-beam Perkin Elmer UV-VIS spectrometer was used to record the transmission and absorbance spectra of spin-coated and printed ZnO films. A blank substrate was placed in line with that reference beam, while the sample spectra were recorded.

Transmission measurements for spin-coated ZnO^0 and AZO show the band edge near 380 nm with a high visible range transparency (**Figure 8**). The individual layering, as observed from

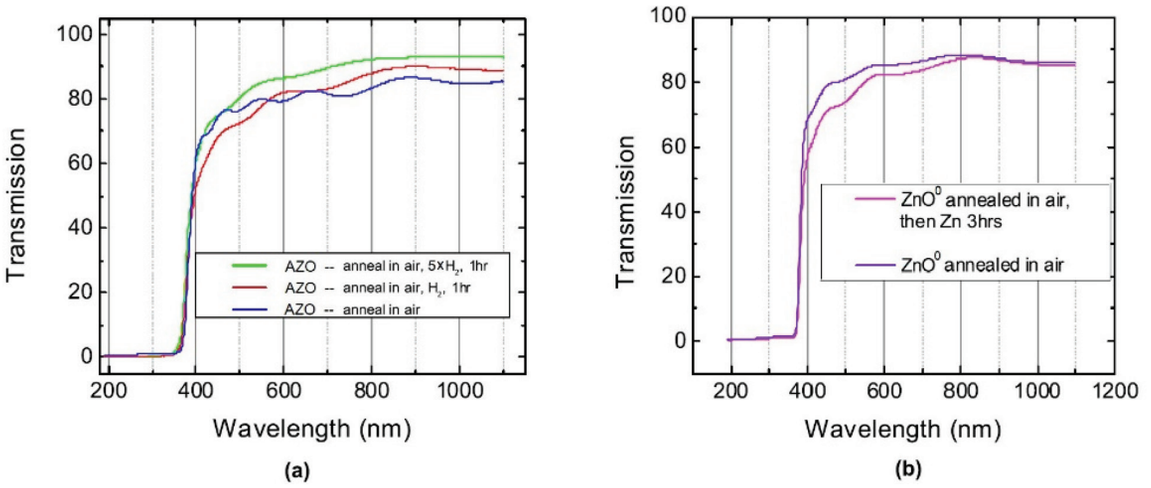

Figure 8. UV-VIS transmission measurements for: (a) AZO films before and after hydrogen treatment at different pressures and (b) ZnO^0 before and after Zn treatment [21].

SEMs, leads to interference effects in the spectra, which can be reduced by a greater H_2 concentration during annealing and lead to improved transparency (**Figure 8a**). This can be explained by a decrease in polycrystallinity observed in XRD analysis. However, the opposite effect occurs after annealing in a Zn environment (**Figure 8b**), which is due to the increase in polycrystallinity.

Printed ZnO and IGZO films also show a band edge near 380 nm from optical absorbance measurements (**Figure 9a**). The bandgap is near 3.2 eV for all printed films, as calculated by the Tauc method (**Figure 9b**). AJP IGZO films are more transparent than IJP films due to better overall print quality. **Figure 10** compares the IJP and AJP techniques, as seen by the naked eye. It is clear that AJP films are more transparent because of less light scattering from surface roughness and striations in the IJP films.

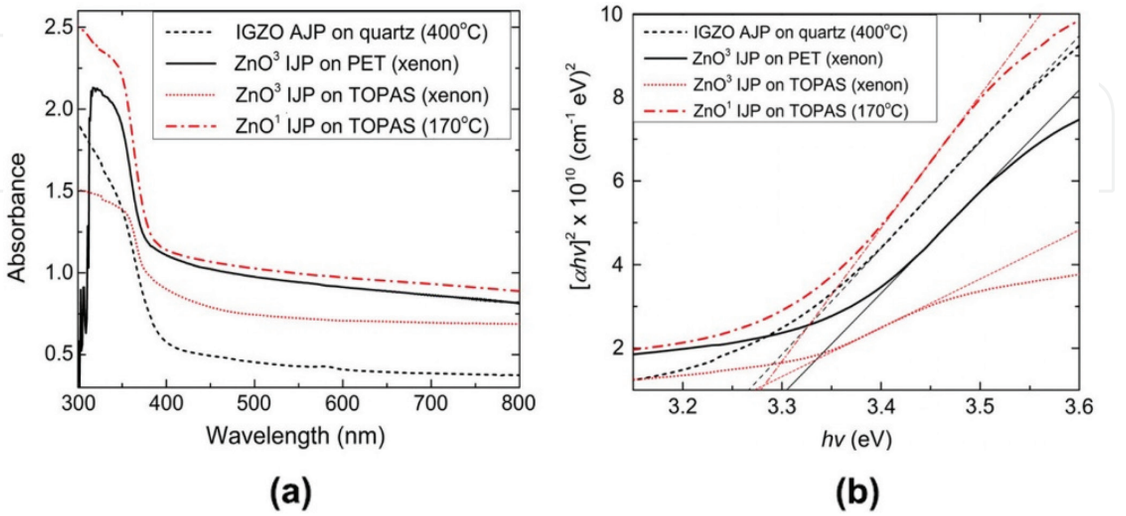

Figure 9. (a) UV-VIS absorbance spectra for IJP and AJP ZnO and IGZO films sintered by different methods, exhibiting a band edge near 380 nm and (b) Tauc plots of direct-bandgap transitions for each spectrum with linear fits extrapolated to $(\alpha hv)^2 = 0$ for bandgap determination [20].

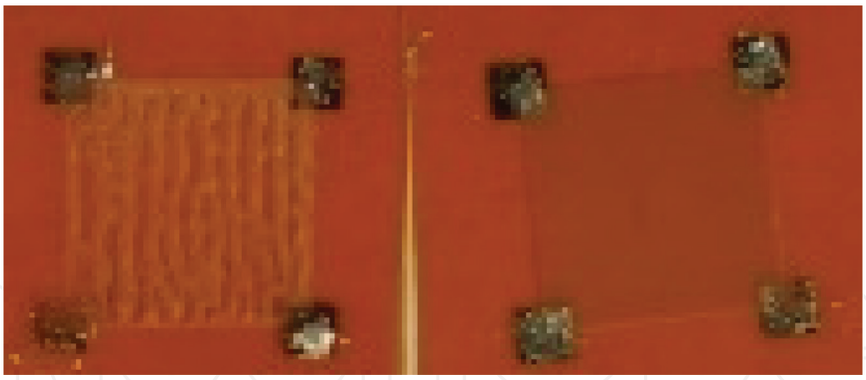

Figure 10. Comparison of ZnO thin films printed by IJP (*left, ZnO*[2]) and AJP (*right, ZnO*[7]) sintered at 300°C. The printed silver pads and indium contacts were applied to the corners for Hall effect measurements. Image taken by a Samsung Galaxy S6 [20].

These results established that the sol-gel precursor method can produce films with good visible range transparency in spin coating and printing techniques. Interference in the visible range absorbance can be reduced by the post-processing conditions. Here, AJP yields a better print quality than IJP and offers similar visible range transparency to spin coating.

8. Van der Pauw and Hall effect measurements

At 300 K, the resistivity was obtained via van der Pauw measurements using an MMR Hall effect system. All spin-coated and printed ZnO, AZO, GZO, and IGZO films show high electrical resistivity after the initial sintering. All spin-coated films were too resistive to initially measure, and the printed films measured resistivity $>10^4$ Ω cm. However, post-processing of spin-coated GZO, AZO, and ZnO^0 in H_2 and Zn environments induced a large conductivity. Van der Pauw and Hall effect measurements for ZnO, AZO, GZO, and IGZO films are summarized in **Table 3**.

AZO thin films annealed in both H_2 and Zn offer the lowest electrical resistivity (1.71×10^{-2} Ω cm) and the highest carrier concentration (3.01×10^{21}). We emphasize that the electrical conductivity results only after the post-processing steps. The large decrease in resistivity is attributed to the passivation of defect states, which will be discussed further in the PAS section of this chapter. The low resistivity coupled with the high visible range transparency offers solution-processed ZnO as a viable option of TCO in printed electronics.

In^{3+} and Ga^{3+} dopants were also investigated through electrical measurements by comparing printed IGZO[2] and ZnO[5] thin films. Both use IJP deposition on Kapton substrates and have a thickness of 600 nm. Unsurprisingly, IGZO[2] has a lower resistivity (3.06×10^4 Ω cm) than ZnO[5] (4.59×10^5 Ω cm). It is well understood that In^{3+} and Ga^{3+} increase conductivity in ZnO, an effect studied in other In- and Ga-doped sol-gel ZnO [32, 33].

The lowest resistivity for AJP ZnO is in the thin film that was annealed at 300°C. The overall resistivity of ZnO depends on its structural properties, which are affected by the oxygen concentration in the film. At higher sintering temperatures, resistivity increases with annealing

Sample	Post-processing conditions	Resistivity (Ω cm)	Mobility ($cm^2 V^{-1} s^{-1}$)	Carrier concentration (cm^{-3})
GZO	400°C, 60 min, H_2	1.03×10^{1}	<1	1.43×10^{19}
GZO	400°C, 60 min, H_2 & 400°C, 60 min, Zn	1.97×10^{-1}	<1	1.44×10^{20}
AZO	400°C, 60 min, H_2 & 400°C, 240 min, Zn	1.71×10^{-2}	<1	3.01×10^{21}
ZnO[0]	400°C, 60 min, H_2/N_2 & 400°C, 180 min, Zn	1.83×10^{-1}	2.94×10^{1}	1.16×10^{18}
ZnO[0]	400°C, 60 min, Zn	1.08×10^{2}	<1	1.86×10^{17}
ZnO[5]	—	4.59×10^{5}	—	—
IGZO[2]	—	3.06×10^{4}	—	—
ZnO[6]	—	1.02×10^{5}	—	—
ZnO[7]	—	8.36×10^{4}	—	—
ZnO[8]	—	2.25×10^{5}	—	—

Table 3. Van der Pauw and Hall effect measurements for ZnO, AZO, GZO, and IGZO thin films grown from ZnO sol-gel precursors, listing the film type, post-processing conditions, resistivity, mobility, and carrier concentration [20, 21].

temperature [34, 35]. However, at temperatures below 300°C, we see the opposite effect [36]. While increasing the sintering temperature, we are removing more solvent, forming a ZnO structure, and increasing the grain size, which creates more pathways for conduction. As we further increase temperature, the grain size continues to increase—as seen in XRD—but more oxygen is being introduced to the ZnO. Increasing the grain size is expected to decrease the resistivity [37], while introducing more oxygen may increase the resistivity [38], resulting in a local minimum in the resistivity as a function of sintering temperature.

In general, doping, sintering, and post-processing all play a vital role in the conductivity of sol-gel ZnO films because of their effects on the ZnO lattice structure and defect formation. First, shallow donors can increase the free carriers in the conduction band. Second, the solvent must be completely evaporated, and the grain boundary concentration and adsorbed oxygen must be minimized to increase the mobility and carrier concentration, respectively. And lastly, post-processing techniques can be utilized to further improve the polycrystallinity and passivate defect charge states.

9. Photoconductivity

The MMR Hall effect system was equipped with a 365-nm light-emitting diode (LED), positioned 1.8 cm from the sample stage, to measure the resistivity as a function of light intensity. After dark measurements were taken, the LED light intensity was increased in steps up to 24 mW (~4.4×10^{16} photons·cm^{-2} s^{-1}), allowing the light and temperature to stabilize for at least 1 min prior to each measurement. Although light from the LED produces localized heating,

http://dx.doi.org/10.5772/intechopen.82041

the temperature was maintained at 300 K using a Joule-Thompson refrigerator located directly beneath the sample stage, operating in combination with a heating element. Photoconductivity was observed in IJP ZnO[5]; IJP IGZO[2]; and AJP ZnO[6], ZnO[7], and ZnO[8] (**Figure 11**).

Upon initial UV LED illumination at 0.98 mW (~4.4×10^{16} photons·cm^{-2} s^{-1}), there is a sharp decrease in resistivity. We credit this to ZnO absorbing light and promoting an electron from the valence band to the conduction band because the incident UV photons are of greater energy (~3.4 eV) than the ZnO bandgap (~3.2 eV). The photoresponse is due to oxygen chemisorption, where light illumination causes oxygen desorption and the release of trapped electrons to the conduction band [39]. Here, the greatest conductive response is seen at the greatest sintering temperature in AJP ZnO. This may be because larger grains desorb more oxygen when illuminated. In addition, the larger grain size would allow for better electron mobility.

With increased light intensity, IJP ZnO thin films quickly saturate, as there is no more oxygen to desorb. But, AJP ZnO—which has a greater photoconductive response—does not saturate at higher light intensity. As the intensity increases, photogenerated holes can be produced and then trapped at charged boundary states, while excess electrons can be promoted to the conduction band, increasing the free carrier concentration. In addition to the effect of the grain boundary, the charge state of defects may also undergo a change upon illumination and

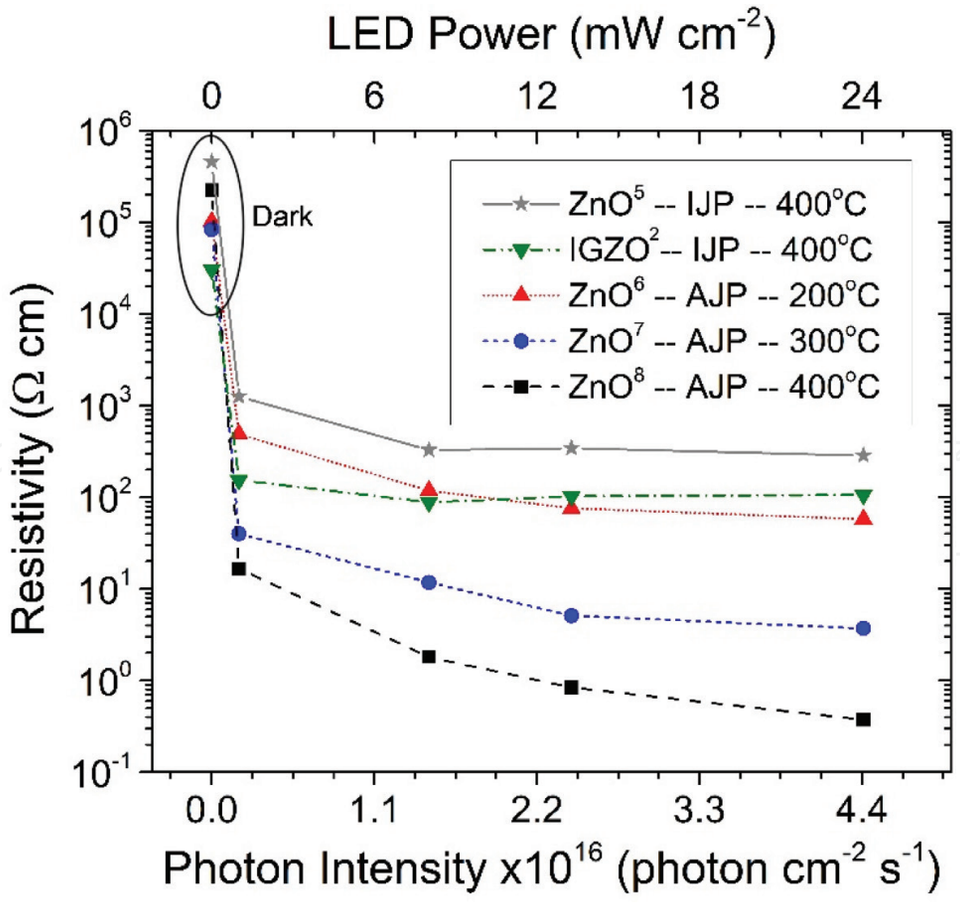

Figure 11. Resistivity measurements of printed ZnO films as a function of light intensity (365-nm LED) [20].

lead to an increase or a decrease in electron scattering affecting electron mobility. For instance, a change in the charge state of defects could increase electron scattering, decreasing the electron mobility and compromising the conductivity. Both the carrier concentration and electron mobility strongly affect the transport properties of ZnO films, and different photo-induced processes could lead to the observed non-linear behavior with increasing light intensity.

10. Positron annihilation spectroscopy

It is impossible to understand the effect of annealing on the transport properties without investigating the presence of point defects in the films. PAS is a well-established technique for measurements of cation vacancies, which strongly influence the transport properties [40–44]. In fact, many works have applied PAS and identified Zn vacancies in ZnO films and bulk single crystals [39–41]. The sensitivity of PAS to open volume defects such as vacancies can be understood as follows. The lack of positive ion cores at vacancies forms an attractive potential that traps positrons leading to characteristic changes in the measured positron annihilation parameters. Therefore, PAS is a very useful tool to further improve the development of sol-gel ZnO film. Here, depth-resolved Doppler broadening of PAS measurements was applied to elucidate the aforementioned effect of annealing on the electrical properties of ZnO films. The measurements were carried out on AZO films before and after annealing in forming gas (5% H_2, 95% N_2). **Figure 12a** and **b** shows S and W parameters, respectively, for the films as a function of incident positron energy and mean implantation depth. The S and W parameters represent the annihilation fraction of positrons with valence and core electrons, respectively, and they provide an indication about defect density [45–47]. The S parameter was obtained from the annihilation peak by dividing the counts in the central peak by the total counts in

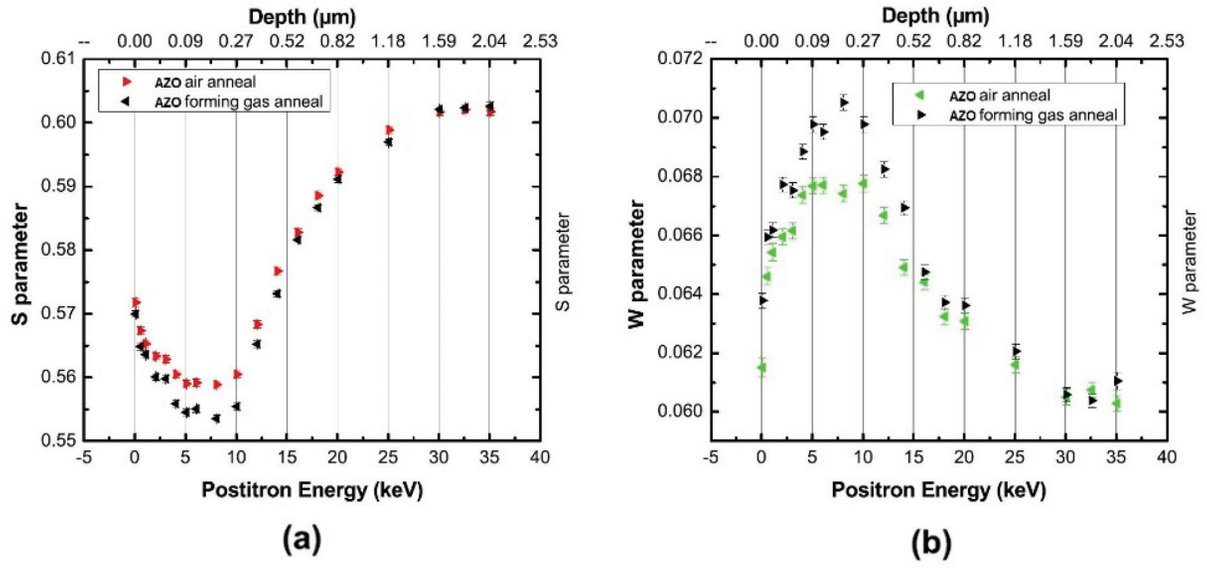

Figure 12. Depth-resolved PAS for AZO before and after forming gas post-processing: (a) S parameter as a function of positron beam energy and mean positron implantation depth and (b) W parameter as a function of positron beam energy and mean positron implantation depth [21].

the peak, while the W parameter was obtained by dividing the counts in the wings of the peak by the total counts in the peak. Trapped positrons at defects are more likely to annihilate with low-momentum valence electrons causing an increase in S parameter and a decrease in W parameter [45–47]. In **Figure 12a** and **b**, an increase in S parameter and a decrease in W parameter at low positron energy (0–5 keV) are due to positron annihilation at the surface of the films. The figures show a significant decrease in S parameter and an increase in W parameter after H_2 processing, which can be interpreted as follows. A Zn vacancy has a negative charge state and is therefore an effective trapping center for positrons, while an O vacancy or interstitial defects cannot trap positrons. Therefore, a decrease in S parameter and an increase in W parameter after H_2-annealing are a clear indication for the reduction or passivation of Zn vacancy-related defects. Annealing in forming gas cannot eliminate Zn vacancies; however, hydrogen can partially or completely fill Zn vacancies modifying their negative charge state, which prevents positron trapping. Similarly, Zn interstitials can fill Zn vacancies decreasing positron trapping. **Figure 13** shows the S-parameter versus W-parameter plot for ZnO films after air annealing, ZnO films after forming gas annealing, and ZnO bulk single crystals. The points on the graph represent the data points corresponding to energy values at which positrons annihilate only in the middle of the film without any influence from the surface or the substrate. The line in the S-parameter versus W-parameter plot runs through the bulk value, which is an indication that there is only one dominant defect type in the samples [40, 46]. This illustrates that H_2 annealing did not create new defects but only reduced Zn vacancies, the dominant trapping defect for positrons in ZnO. PAS studies here illustrated that Zn vacancy-related defects are dominant in sol-gel ZnO films and provided strong evidence that hydrogen passivates Zn vacancies, eliminating their deep acceptor state, which leads to a large increase in carrier concentration and high-induced conductivity in the films.

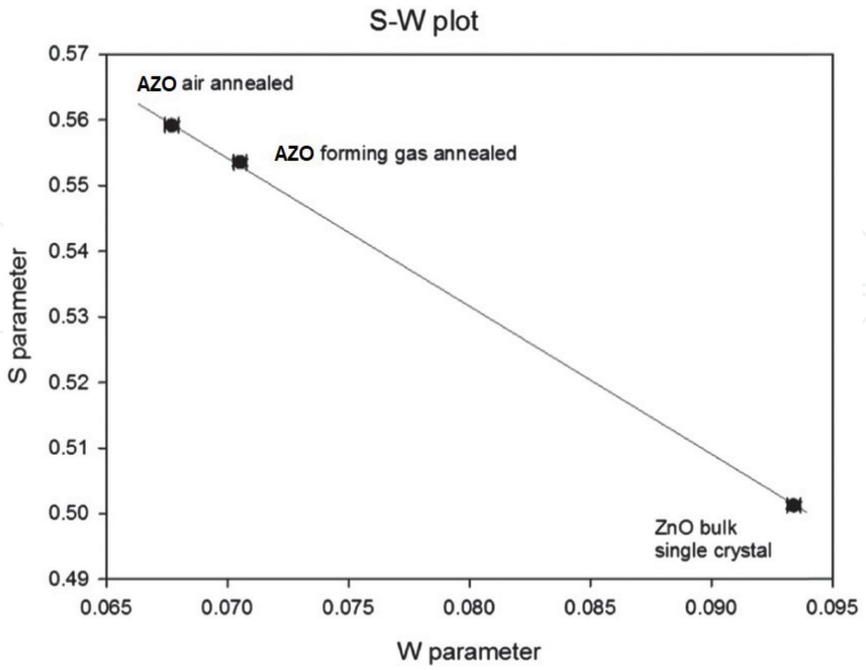

Figure 13. S-parameter versus W-parameter plot for bulk ZnO single crystal and AZO before and after processing in forming gas. The three points lie on a straight line, indicating one dominant defect type [21].

11. Conclusion

In conclusion, ZnO films were deposited on various substrates using a simple sol-gel precursor method. This precursor has proven compatible spin coating, IJP, and AJP techniques to fabricate TCOs and photodetectors. SEM measurements reveal surface roughness and non-uniformity that are inherent to the sol-gel process. However, these drawbacks can be overcome to optimize the UV-VIS and electrical properties. XRD analysis shows polycrystallinity that can be tuned by sintering temperature and processing atmosphere. The post-processing step and the addition of In^{3+} and Ga^{3+} have both shown to enhance the electrical conductivity of ZnO either through the suppression of acceptor vacancies or the addition of shallow donors. Resistive ZnO thin films also exhibited an overall photoconductive response of 10^6. PAS was executed to study the role of hydrogen passivation of cation vacancies in the electrical properties of sol-gel ZnO thin films and to illustrate its need for the development of conductive sol-gel ZnO films. Overall, this work demonstrates the compatibility of sol-gel ZnO with printed electronics and other devices and presents fundamental research to understand the structural, optical, and electrical properties of the material system.

Acknowledgements

The authors would like to thank the following collaborators for their contributive efforts: Wolfgang Anwand and Andreas Wagner at the Institute of Radiation Physics; Pooneh Saadatkia, Erik Flesburg, and Micah Haseman at Bowling Green State University; and Emily M. Heckman, Eric Kreit, Roberto S. Aga, Brett Wenner, Kevin Leedy, Steve Tetlak, David C. Look, Jeff Allen, and Monica Allen at the Air Force Research Laboratories at Wright-Patterson Air Force Base and Eglin Air Force Base.

Funding for this work was provided by multiple AFRL and DAGSI projects.

Conflict of interest

The authors declare that they have no conflicts of interest.

Author details

David Winarski[1,2] and Farida Selim[1,2]*

*Address all correspondence to: faselim@bgsu.edu

1 Department of Physics and Astronomy, Bowling Green State University, Bowling Green, Ohio, USA

2 Center for Photochemical Sciences, Bowling Green State University, Bowling Green, Ohio, USA

References

[1] Petti L, Münzenrieder N, Vogt C, Faber H, Büthe L, Cantarella G, et al. Metal oxide semiconductor thin-film transistors for flexible electronics. Applied Physics Reviews. 2016;**3**(2):021303

[2] Choi C-H, Lin L-Y, Cheng C-C, Chang C-H. Printed oxide thin film transistors: A mini review. ECS Journal of Solid State Science and Technology. 2015;**4**(4):3044-3051

[3] Smith M, Choi YS, Boughey C, Kar-Narayan S. Controlling and assessing the quality of aerosol jet printed features for large area and flexible electronics. Flexible and Printed Electronics. 2017;**2**(1):015004

[4] Teng L, Plötner M, Türke A, Adolphi B, Finn A, Kirchner R, et al. Nanoimprint assisted inkjet printing to fabricate sub-micron channel organic field effect transistors. Microelectronic Engineering. 2013;**110**:292-297

[5] Yin Z, Huang Y, Bu N, Wang X, Xiong Y. Inkjet printing for flexible electronics: Materials, processes and equipments. Chinese Science Bulletin. 2010;**55**(30):3383-3407

[6] Mohammed MG, Kramer R. All-printed flexible and stretchable electronics. Advanced Materials. 2017;**29**:1604965

[7] Liu Y-F, Tsai M-H, Pai Y-F, Hwang W-S. Control of droplet formation by operating waveform for inks with various viscosities in piezoelectric inkjet printing. Applied Physics A. 2013;**111**(2):509-516

[8] Eckstein R, Rödlmeier T, Glaser T, Valouch S, Mauer R, Lemmer U, et al. Aerosol-jet printed flexible organic photodiodes: Semi-transparent, color neutral, and highly efficient. Advanced Electronic Materials. 2015;**1**(8):1500101

[9] Aga RS, Lombardi JP, Bartsch CM, Heckman EM. Performance of a printed photodetector on a paper substrate. IEEE Photonics Technology Letters. 2014;**26**(3):305-308

[10] Lombardi JP, Bartsch CM, Aga RS, Heckman EM. Characterisation of DNA biopolymer-based UV photodetector fabricated by inkjet printing. Electronics Letters. 2015;**51**(10):778-780

[11] Girgis E, Fang M, Hassan E, Kathab N, Rao K. Ink-jet-printed $(ZnO)_{1-x}(TiO2)_x$ composite films for solar cell applications. Journal of Materials Research. 2012;**28**(03):502-506

[12] Liang YN, Lok BK, Wang L, Feng C, Lu ACW, Mei T, et al. Effects of the morphology of inkjet printed zinc oxide (ZnO) on thin film transistor performance and seeded ZnO nanorod growth. Thin Solid Films. 2013;**544**:509-514

[13] Oh S, Nagata T, Volk J, Wakayama Y. Nanoimprint for fabrication of highly ordered epitaxial ZnO nanorods on transparent conductive oxide films. Applied Physics Express. 2012;**5**(9):095003

[14] Meier M, Paetzold UW, Prömpers M, Merdzhanova T, Carius R, Gordijn A. UV nanoimprint for the replication of etched ZnO:Al textures applied in thin-film silicon solar cells. Progress in Photovoltaics: Research and Applications. 2013;**22**(12):1226-1236

[15] Hartner S, Khalil A, Ali M, Winterer M, Wiggers H. Ink-jet printed ZnO nanoparticles thin film for sensing applications. In: NSTI-Nanotech. Vol. 2. Boca Raton: CRC Press; 2010. pp. 535-537

[16] Brinker CJ, Scherer GW, editors. Sol–Gel Science: The Physics and Chemistry of Sol–Gel Processing. Saint Louis: Elsevier Science; 2014. p. 912

[17] Reisfeld R. Sol gel processed lasers. In: Sakka S, editor. Sol–Gel Technology (Handbook) 3. Dordrecht: Kluwer Anademic Publishers; 2004. pp. 239-261

[18] Reisfeld R. Doped polymeric system produced by sol–gel technology: Optical properties and potential industrial application. Polymer. 2005;**5**:95-103

[19] Reisfeld R, Saraidarov T. Innovative materials based on sol–gel technology. Optical Materials. 2006;**28**(1-2):64-70

[20] Winarski DJ, Kreit E, Heckman EM, Flesburg E, Haseman M, Aga RS, et al. Photoconductive ZnO Films Printed on Flexible Substrates by Inkjet and Aerosol Jet Techniques. Journal of Electronic Materials. 2017;**47**(2):949-954

[21] Winarski DJ, Anwand W, Wagner A, Saadatkia P, Selim FA, Allen M, et al. Induced conductivity in sol–gel ZnO films by passivation or elimination of Zn vacancies. AIP Advances. 2016;**6**(9):095004

[22] Mukhamedshina D, Mit' K, Chuchvaga N, Tokmoldin N. Fabrication and study of sol–gel ZnO films for use in Si-based heterojunction photovoltaic devices. Modern Electronic Materials. 2017;**3**(4):158-161

[23] Muslih EY, Munir B. Fabrication of ZnO thin film through chemical preparations. In: Ameen S, Akhtar MS, Shin H-S, editors. Emerging Solar Energy Materials. London: IntechOpen Limited; 2018. pp. 45-57

[24] Mahmood A, Naeem A. Sol-gel-derived doped ZnO thin films: Processing, properties, and applications. In: Chandra U, editor. Recent Applications in Sol–Gel Synthesis. London: IntechOpen Limited; 2017. pp. 169-193

[25] Znaidi L, Touam T, Vrel D, Souded N, Yahia S, Brinza O, et al. AZO thin films by sol–gel process for integrated optics. Coatings. 2013;**3**(3):126-139

[26] Liu Y, Li Y, Zeng H. ZnO-based transparent conductive thin films: Doping, performance, and processing. Journal of Nanomaterials. 2013;**2013**:196521

[27] Wang F-H, Chou C-T, Kang T-K, Huang C-C, Liu H-W, Kung C-Y. Structural, electrical, and optical properties of carbon nanotube-incorporated Al-doped zinc oxide thin films prepared by sol–gel method. Journal of Ceramic Processing Research. 2014;**14**:149-152

[28] Zhang X, Lee H, Kwon J-H, Kim E-J, Park J. Low-concentration indium doping in solution-processed zinc oxide films for thin-film transistors. Materials. 2017;**10**(8):880

[29] Khranovskyy V, Grossner U, Lazorenko V, Lashkarev G, Svensson BG, Yakimova R. PEMOCVD of ZnO thin films, doped by Ga and some of their properties. Superlattices and Microstructures. 2006;**39**(1-4):275-281

[30] Yadav AB, Periasamy C, Jit S. Study of post annealing effects on structural and optical properties of sol–gel derived ZnO thin films grown on n-Si substrate. In: Proceedings of IOP Conference Series: Materials Science and Engineering (ICMST '12); 10-14 June 2012; Kerala. New York: IOP Publishing; 2015. p. 012060

[31] López-Mena E, Jiménez-Sandoval S, Jiménez-Sandoval O. ZnO thin films prepared at low annealing temperatures, from a novel, simple sol–gel precursor solution. Journal of Sol-Gel Science and Technology. 2015;**74**(2):419-424

[32] Bel-Hadj-Tahar R, Mohamed AB. Sol–Gel processed indium-doped zinc oxide thin films and their electrical and optical properties. New Journal of Glass and Ceramics. 2014;**04**(04):55-65

[33] Nayak PK, Kim J, Chung S, Jeong J, Lee C, Hong Y. Spin-coated Ga-doped ZnO transparent conducting thin films for organic light-emitting diodes. Journal of Physics D: Applied Physics. 2009;**42**(13):139801

[34] Asghar M, Noor H, Awan M, Naseem S, Hasan M-A. Post-annealing modification in structural properties of ZnO thin films on p-type Si substrate deposited by evaporation. Materials Science in Semiconductor Processing. 2008;**11**(1):30-35

[35] Bouhssira N, Abed S, Tomasella E, Cellier J, Mosbah A, Aida M, et al. Influence of annealing temperature on the properties of ZnO thin films deposited by thermal evaporation. Applied Surface Science. 2006;**252**(15):5594-5597

[36] Shariffudin SS, Mamat MH, Herman SH, Rusop M. Influence of drying temperature on the structural, optical, and electrical properties of layer-by-layer ZnO nanoparticles seeded catalyst. Journal of Nanomaterials. 2012;**2012**:1-7

[37] Khan M, Bhatti K, Qindeel R, Alonizan N, Althobaiti HS. Characterizations of multilayer ZnO thin films deposited by sol–gel spin coating technique. Results in Physics. 2017;**7**:651-655

[38] Aghamalyan NR, Gambaryan IA, Goulanian EK, Hovsepyan RK, Kostanyan RB, Petrosyan SI, et al. Influence of thermal annealing on optical and electrical properties of ZnO films prepared by electron beam evaporation. Semiconductor Science and Technology. 2003;**18**(6):525-529

[39] Takahashi Y, Kanamori M, Kondoh A, Minoura H, Ohya Y. Photoconductivity of ultrathin zinc oxide films. Japanese Journal of Applied Physics. 1994;**33**(Part 1, No. 12A):6611-6615

[40] Krause-Rehberg R, Leipner HS. Positron Annihilation in Semiconductors: Defect Studies. Berlin: Springer; 1999. p. 383

[41] Selim FA, Winarski D, Varney CR, Tarun MC, Ji J, MD MC. Generation and characterization of point defects in $SrTiO_3$ and $Y_3Al_5O_{12}$. Results in Physics. 2015;**5**:28-31

[42] Čížek J, Valenta J, Hruška P, Melikhova O, Procházka I, Novotný M, et al. Origin of green luminescence in hydrothermally grown ZnO single crystals. Applied Physics Letters. 2015;**106**:251902

[43] Brillson LJ, Zhang Z, Doutt DR, Look DC, Svensson BG, Yu A. Interplay of dopants and native point defects in ZnO. Physica Status Solidi B. 2013;**250**:2110-2113

[44] Selim FA, Weber MH, Solodovnikov D, Lynn KG. Nature of native defects in ZnO. Physical Review Letters. 2007;**99**(8):085502

[45] Hautojäervi P. Positrons in Solids. Heidelberg: Springer; 1979. p. 258

[46] Schultz P, Lynn KG. Interaction of positron beams with surfaces, thin films, and interfaces. Reviews of Modern Physics. 1988;**60**(3):701-779

[47] Selim FA, Wells DP, Harmon JF, Williams J. Development of accelerator-based γ-ray-induced positron annihilation spectroscopy technique. Journal of Applied Physics. 2005;**97**:113539